Check for updates

Inducing tumor ferroptosis *via* a pH-responsive NIR-II photothermal agent initiating lysosomal dysfunction†

Zhiwei Zhang, ‡[a,b,c] Jingjing Xiang,‡[b,c] Lijiao Guan,‡[a] Pu Chen,[d] Changzhong Li,[e] Chunlei Guo,[e] Yan Hu,*[e] Saipeng Huang, *[a] Lintao Cai *[b,c] and Ping Gong*[b,c]

Ferroptosis is a unique programmed cell death process that was discovered a few years ago and plays an important role in tumor biology and treatment. However, it still remains a challenge to modulate tumor ferroptosis by spatiotemporally controlled cell-intrinsic Fenton chemistry. Herein, a pH activated photothermal sensitizer IR-PE has been designed and synthesized on the basis of cyanine bearing a diamine moiety, which is capable of triggering the lysosomal dysfunction-mediated Fenton pathway under the irradiation of near-infrared light to evoke ferroptosis, thereby improving antitumor efficacy and mitigating systemic side effects.

Introduction

Ferroptosis is a process that relies on the Fenton reaction between ferrous ions (Fe^{2+}) and hydrogen peroxide (H_2O_2) in an acidic environment. This reaction generates harmful hydroxyl free radicals ($^{\bullet}OH$) and results in lipid peroxidation, ultimately leading to the death of tumor cells.[1–3] Due to its potential, ferroptosis has garnered significant interest within the cancer research community as it offers an alternative strategy for anti-tumor treatment. The current approach to cancer therapy involving ferroptosis primarily relies on the introduction of exogenous iron-based nanomaterials. However, the excessive use of exogenous iron and inorganic materials has raised significant biosafety concerns.[4–7] Consequently, one of the major challenges in current ferroptosis research is finding

ways to induce ferroptosis without relying on ferrous materials.

It is known that lysosomes have emerged as important organelles to specifically target tumor cells in cancer treatment, and related iron autophagy can regulate intracellular iron metabolism.[8] The pH of lysosomes is about 3.8 to 4.7, which is beneficial for accelerating the release of catalytic ions.[9,10] Despite the appropriate pH of lysosomes for the Fenton reaction, the efficiency of ferroptosis is low due to insufficient H_2O_2 levels and autophagy repair within the lysosomes.[11] Additionally, it has been found that lysosome dysfunction can lead to lysosome membrane permeability, resulting in the release of various substances, such as H^+ and Fe^{2+}, into the cytoplasm.[8] This indicates that enhancing the intrinsic Fenton reaction efficiency of cells by regulating lysosome function may offer a new alternative to triggering ferroptosis. However, the chemotherapeutics bring serious side effects to normal tissues due to the lack of tumor specificity[12–14] and spatiotemporal controllability when regulating lysosome function.[15–18] To overcome this drawback, it is imperative to develop a non-metallic ferroptosis inducer with both spatiotemporal regulation and tumor specificity, which has important scientific significance for future anti-tumor treatment research based on ferroptosis.[19]

To solve the above problems, we have developed an easily synthesized pH responsive NIR photothermal agent, IR-PE, which can achieve the spatiotemporal control of lysosome dysfunction to trigger the Fenton reaction and subsequent ferroptosis under near infrared laser irradiation. In this system, IR-PE would target the lysosomes of tumor cells and the photothermal effect activated by the acid microenvironment of the lysosomes can cause lysosome dysfunction under 808 nm light, including membrane permeability, cytoplasmic acidification and autophagy damage. More importantly, the lysosome dysfunction mediated by IR-PE under light activation significantly enhances the Fenton reaction in tumor cells and causes ferroptosis, thus improving the anti-tumor efficacy and reducing the damage to normal tissues (Scheme 1).

[a]*Northwest University, Xi'an 710069, China. E-mail: huangsaipeng@nwu.edu.cn*
[b]*Guangdong Key Laboratory of Nanomedicine, CAS-HK Joint Lab for Biomaterials, CAS Key Lab for Health Informatics, Sino-Euro Center of Biomedicine and Health, Shenzhen Institutes of Advanced Technology, Chinese Academy of Sciences, Shenzhen 518055, China. E-mail: lt.cai@siat.ac.cn, ping.gong@siat.ac.cn*
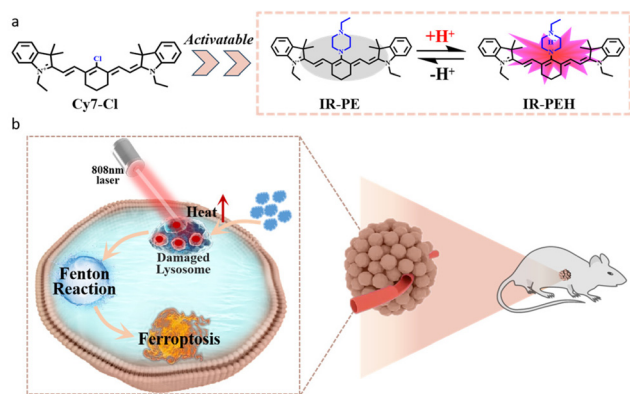[c]*University of Chinese Academy of Sciences, Beijing 100049, China*
[d]*Baoji University of Arts and Sciences, Baoji 721013, China*
[e]*Peking University Shenzhen Hospital, No. 1120, Lianhua Road, Shenzhen 518036, China. E-mail: huyan96105@126.com*
†Electronic supplementary information (ESI) available. See DOI: https://doi.org/10.1039/d3nr04124g
‡These authors contributed equally to this work.

Scheme 1 (a) The chemical structures of IR-PE and IR-PEH and the proposed reversible conversion in response to the H$^+$ redox cycle. (b) Schematic illustration of the current strategy for spatiotemporally controlled tumor ferroptosis *via* the pH-responsive photosensitizer IR-PE.

Results and discussion

IR-PE was readily synthesized following the procedures outlined in Fig. S1,† and the resulting product was comprehensively characterized using ^{1}H and ^{13}C NMR spectroscopy as well as HRMS (Fig. S2–S4†). With the probe in hand, we first evaluated the spectral response of IR-PE, and we found that when the pH changed from 6.5 to 3.5, the absorption and fluorescence (791 nm and 917 nm) reached their maximum correspondingly (Fig. 1a–d). Furthermore, the corresponding product was also confirmed to be IR-PEH by the mass spectrum, in which the peak was found at 295 in accordance with the doubly charged ion peak at 590 (Fig. S5†). The calculations

Fig. 1 Photophysical and photothermal properties of IR-PE. (a) Emission spectra of 5 μg mL^{-1} IR-PE at various pH values upon excitation at 750 nm. (b) Fluorescence intensity of IR-PE at 791 nm and (c) 917 nm in PBS with different pH values. (d) UV-Vis spectra of 5 μg mL^{-1} IR-PE at various pH values in PBS buffer. (e) Temperature curves of 10 μg mL^{-1} IR-PE in PBS with different pH values after continuous laser irradiation for 10 minutes. Inset: photothermal images of IR-PE in PBS with different pH values after continuous laser irradiation for 10 minutes (pH values in b–e: 3.5, 4, 4.5, 4.7, 4.8, 4.9, 5, 5.1, 5.2, 5.4, 5.7, and 6.5). (f) The photothermal stability study of 10 μg mL^{-1} IR-PE in PBS (pH 3.5) by repeated 808 laser irradiation for 5 cycles (10 min of laser on and then naturally cooled to room temperature in each cycle).

of the highest occupied molecular orbital (HOMO) and the lowest-unoccupied molecular orbital (LUMO) electrons showed that IR-PE (2.075 eV) has a larger energy gap than IR-PEH (1.951 eV), which was consistent with the absorbance wavelength shift of IR-PE and IR-PEH (Fig. S6† and Fig. 1d). Meanwhile, IR-PE showed excellent pH reversibility by alternately changing the pH between 3.5 and 6.5 even after five cycles (Fig. S7†). Moreover, the drastically increased absorption in the NIR region made IR-PEH an efficient photothermal sensitizer. As demonstrated in Fig. 1e, the photothermal efficiency reached its maximum when the pH fell below 4.7. Besides, upon irradiation with 808 nm lasers (0.1 W cm^{-2}), the temperature of the IR-PE solution exhibited a dramatic increase from 25.6 to 52.6 °C, showing a higher photothermal conversion efficiency (20.05%) than indocyanine green (ICG, a common NIR photothermal agent) (5.22%) (Fig. S8†). However, no photodynamic properties of IR-PE were observed using 1,3-diphenyliso-benzofuran (DPBF) as a reactive oxygen species (ROS) indicator (Fig. S9†). Next, the photothermal stability of IR-PE in PBS (pH 3.5) was evaluated, and the temperature variation of the IR-PE solution was monitored upon irradiation of the solution with an 808 nm laser (0.1 W cm^{-2}) for 10 min and then naturally cooled to room temperature. As shown in Fig. 1f, following five cycles of laser irradiation, there were no noticeable changes in both the temperature value and the rate of temperature increase for the IR-PE solution. Overall, the high photothermal performance and excellent stability of IR-PE make it an encouraging photothermal agent for PTT both *in vitro* and *in vivo*.

We then proceeded to measure the cytotoxicity of IR-PE by the CCK-8 assay. As expected, IR-PE displayed reasonable cytotoxicity toward A549 cells under dark conditions even at 35 μg mL^{-1} (Fig. S10†). To confirm the role of lysosomes in the cell death process induced by IR-PE under NIR light activation, we examined the subcellular distribution of IR-PE in both Hep G2 and A549 tumor cells. Through colocalization imaging, we found that IR-PE showed a strong ability to localize within lysosomes. This capability is likely a result of its protonation and entrapment mechanism, which resembles those of lysosome-targeting compounds and nanoparticles during endocytosis. In simpler terms, IR-PE can effectively accumulate within lysosomes, possibly because it shares a mechanism of entry similar to certain compounds known to target these cellular structures, including the uptake mechanism of nanoparticle entry into cells. To verify the switched-on fluorescence of IR-PE in the acidic lysosomal lumen, A549 cells were treated with bafilomycin A1 (Baf A1), a selective inhibitor of vacuolar-type H$^+$ ATPase (V-ATPase), keeping the acidity of lysosomes by actively pumping in H$^+$.[20,21] After being incubated with 50 nM Baf A1 for 1 hour, the fluorescence of the lysosomes decreased dramatically, which could be interpreted as the basification of the lysosomal lumen. The above studies not only confirmed the specific accumulation of IR-PE into the lysosomes of tumor cells, but also verified that IR-PE specifically lightened the lysosomes of tumor cells by sensing their acidic pH (Fig. 2a). To further elucidate the mechanism of IR-PE-induced
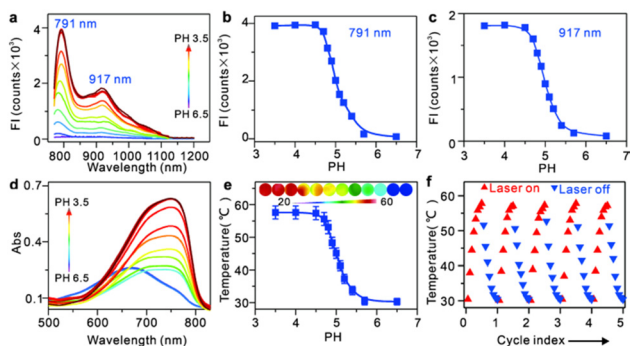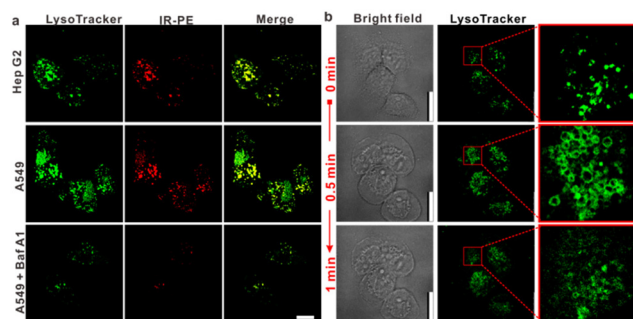
Fig. 2 Lysosomal dysfunction induced by IR-PE upon NIR light activation. (a) Laser scanning confocal microscopy images of live hepatic Hep G2 and A549 tumor cells with IR-PE (red) and a lysosomal marker (green). LSCM images of A549 tumor cells after the treatment of IR-PE in the absence or presence of 50 nM bafilomycin A1. Bars: 10 μm. (b) Time lapse LSCM imaging of Hep G2 tumor cells under 808 nm laser irradiation (0.1 W cm^{-2}) after 5 μg mL^{-1} IR-PE incubation for 3 h (green: LysoTracker® Green, a lysosomal marker). Bars: 25 μm.

selective cancer cell death *via* hyperthermia, LSCM imaging was performed in live Hep G2 tumor cells. Notably, under 808 nm laser irradiation (0.1 W cm^{-2}), the simple tiny spherical sac-like structures of the lysosomes in Hep G2 tumor cells varied remarkably with the loss of membrane integrity and the formation of bubble-like structures (Fig. 2b), which are characteristic of the onset of apoptosis.[22–25]

To verify that the lysosomal dysfunction triggered by NIR photoactivation of IR-PE contributes to the occurrence of ferroptosis,[26] we then investigated the accumulation of cellular ROS and lipid peroxidation (LPO),[27,28] which are the obvious characteristics when ferroptosis occurs. Therefore, we started with the examination of the intracellular ROS levels with a well-recognized ROS probe DCFH-DA, and the confocal imaging results showed that the A549 cells treated with IR-PE under NIR light irradiation exhibited significantly enhanced green fluorescence (Fig. 3a). We proceeded to perform confocal imaging to visualize intracellular ·OH levels, utilizing the well-established indicator coumarin-3-carboxylic acid (3-CCA), and we found negligible fluorescence from 3-CCA without NIR light irradiation, but a significant increase in fluorescence was evident following irradiation with an 808 nm laser (Fig. 3b). These data revealed that NIR light activation of IR-PE to induce intracellular ·OH production is an important mechanism for ferroptosis through the enhanced Fenton reaction. Subsequently, we investigated the lipid peroxide levels with Liperfluo (a commercial LPO assay), which is also an important marker of ferroptosis.[3] As expected, the imaging results suggested that the green fluorescence of IR-PE under 808 nm light irradiation was significantly stronger than that of the control group (Fig. 3c), which demonstrates the noticeable accumulation of lipid peroxide in A549 cells. Furthermore, the intracellular malondialdehyde (MDA) level was also increased with the treatment of IR-PE and NIR irradiation, which is considered to be the end product of LPO and has a positive regulation effect on ferroptosis (Fig. 3d).[29] In contrast, the substan-
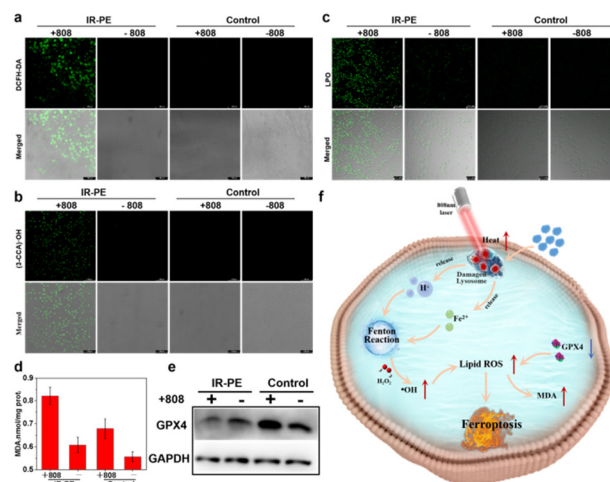

Fig. 3 Evoking ferroptosis *via* the endogenous Fenton reaction induced by IR-PE upon NIR light activation. CLSM images of intracellular ROS (a), ·OH (b) and LPO (c) levels in A549 cells after different treatments, control (without any treatment) or control + 808 nm laser irradiation (0.1 W cm^{-2}, 5 min), IR-PE (5 μg mL^{-1}) or IR-PE (5 μg mL^{-1}) with 808 nm laser irradiation (0.1 W cm^{-2}, 5 min). Scale bar: 100 μm. (d) Intracellular MDA content for cells treated with IR-PE. (e) Intracellular GPX4 protein levels by western blotting assay for cells treated with IR-PE. (f) Schematic illustration of NIR light activation of IR-PE triggering lysosomal dysfunction to promote the Fenton reaction and subsequent ferroptosis.

tial downregulation of GPX4 in IR-PE + NIR irradiation-treated cells was found by western blot analysis, which is another ferroptosis-associated key characteristic (Fig. 3e), suggesting that GPX4 was depleted owing to the extensive lipid oxidation in ferroptosis. In a word, all the results indicated that lysosomal dysfunction was triggered by NIR light-activated IR-PE, which further accelerated the inherent Fenton mechanism of cells to provoke ferroptosis (Fig. 3f).

To assess the effectiveness of IR-PE at detecting viable cancer cells in living organisms, we conducted continuous imaging of mice and monitored cancer cell proliferation in real-time using IR-PE. In this study, mice were initially subcutaneously implanted with varying numbers of live Hep G2 cells, then IR-PE was injected *in situ* at a dosage of 40 mg kg^{-1}, and then we performed imaging at specific time points ranging from 1 to 48 hours after cell injection. The results, as depicted in Fig. 4a, showed that when 10^4 Hep G2 cells were injected, a robust fluorescence signal was detected at the cell injection site after 1 hour. Even with the injection of 10^4 and 10^3 cells, the fluorescence signal remained detectable at 24 and 20 hours, respectively. However, no signal was detected when only 10 cells were injected. Furthermore, when quantifying the photon counts in the cell-injected region for different amounts of Hep G2 cells at each time point, we observed a positive correlation between the increase in signal intensity and the higher number of injected cells (Fig. 4b). To illustrate the relationship between the fluorescence signal intensity at the tumor site and the number of tumor cells more intuitively,
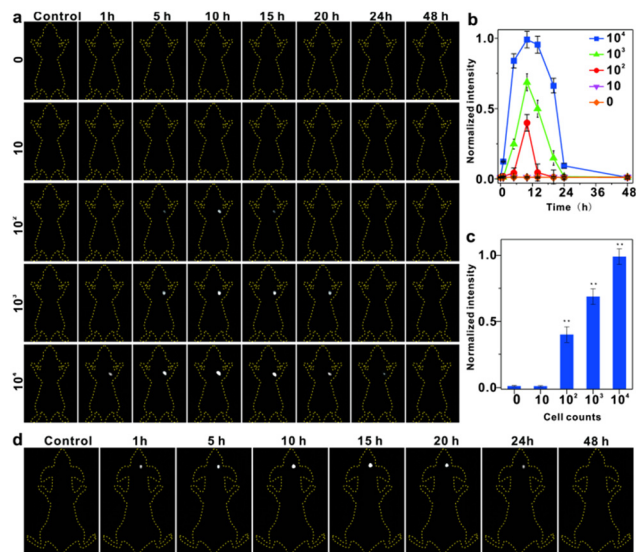
Fig. 4 Cancer cell detection limit and sensitivity of IR-PE *in vivo*. (a) Fluorescent images of mice subcutaneously injected with different numbers of Hep G2 cells (*i.e.*, 10^4, 10^3, 10^2, 10 and 0 cells in 200 μL PBS). The cancer cells were implanted in the armpit, while IR-PE was injected *in situ*. (b) The fluorescence intensity of the Hep G2 cell-injected regions at indicated time points. $n = 5$. (c) The fluorescence intensity of the Hep G2 cell-injected regions at 10 h after injection of IR-PE. $n = 5$, *$P < 0.05$, **$P < 0.01$. (d) Fluorescent images of orthotopic U87MG human glioblastoma tumor-bearing mice.

we measured the fluorescence intensity of the Hep G2 cell-injected regions at 10 hours after IR-PE injection. The results revealed that as the number of tumor cells increased, the fluorescence intensity of the tumor site also increased (Fig. 4c). Additionally, we established an orthotopic U87MG human glioblastoma mouse model to evaluate the *in vivo* tumor accumulation of IR-PE using fluorescent imaging. After the intratumoral injection of IR-PE, the fluorescence signal in the tumor tissues gradually increased, reaching its peak at 15 hours after injection. Moreover, the NIR-II fluorescence signals disappeared by 24 h (Fig. 4d). These findings indicated that IR-PE could effectively track *in vivo* tumors.

Encouraged by the excellent photothermal effect of IR-PE *in vitro*, we initiated an evaluation of its pH-dependent photothermal characteristics in mice. Specifically, two A549 tumors were established, one on the left hind leg (tumor 1, the untreated group) and another on the right hind leg (tumor 2, injected with a Baf A1 solution to upregulate the tumor's pH). 10 hours post administration of IR-PE injection, we found that the temperature of tumor 1 rose to 58 °C after 808 nm laser irradiation, which was significantly higher than that of tumor 2 (Fig. S11†). The outcomes affirmed that IR-PE was suitable for photothermal therapy of tumors *in vivo*. Subsequently, we explored the potential of IR-PE to treat tumors in mice carrying A549 tumors. 5×10^5 A549 cells in PBS buffer were injected into the right flanks of each female BALB/c mouse to establish an A549 tumor bearing mouse model. After about 9 days, mice

with tumor volumes at about 90 mm³ were used for further experiments. Then the mice were randomly divided into four groups, which were saline, saline + laser, IR-PE (0.1 mM), IR-PE (0.1 mM) + laser. The therapeutic effect was examined through intratumoral injection, and two groups of mice were illuminated by an 808 nm laser at a power density of 0.1 W cm⁻² for a continuous duration of 20 minutes. After 24 h of different treatments, the survival rate and tumor volume of the remaining mice in each group were monitored for 30 days. Remarkably, tumors grew rapidly in the saline, saline + laser and IR-PE groups, while tumors in the IR-PE + laser group were significantly inhibited (Fig. 5a). Moreover, during the treatment, the IR-PE + laser group demonstrated a superior survival rate compared to the other three groups (Fig. 5b). All the results indicated that NIR photoactivation of IR-PE greatly enhanced the antitumor effect *in vivo*. Following the treatment, we conducted H&E staining on major organs taken from mice in each group to assess the organ toxicity induced by IR-PE. As expected, there were no observable signs of organ damage or inflammatory lesions in any of the groups (Fig. 5c). These results further confirmed that the administered dose of IR-PE was well-tolerated, and there were no detectable acute side effects in the tested mice. The studies provided strong evidence that IR-PE is a biocompatible small molecule capable of delivering highly effective photothermal therapy without causing significant adverse effects at the tested doses following intratumoral administration.
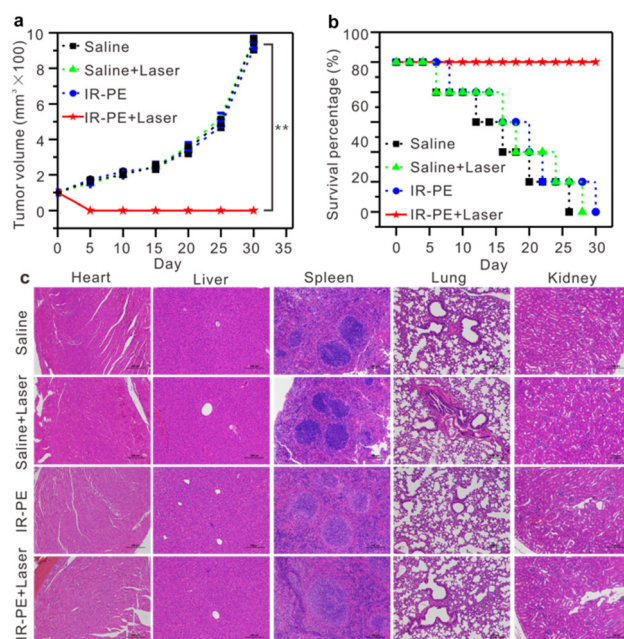

Fig. 5 *In vivo* photothermal therapy of IR-PE. (a) The tumor growth curve within 30 days in different groups. The data are shown as mean ± SD ($n = 10$), *$P < 0.05$, **$P < 0.01$. (b) Survival rate profiles of mice bearing A549 tumors within 30 days in different groups. (c) H&E stained images of A549 tumor sections collected from different groups of mice 24 hours post-treatment. Scale bar: 200 μm.

Conclusions

In summary, we have developed a pH-responsive molecule that can promote the intrinsic Fenton reaction in tumor cells under the irradiation of NIR light. At the same time, the acid-activatable photothermal properties of IR-PE also exhibited strong antitumor efficacy with minimal off-tumor toxicity. This study provided a novel non-metallic ferroptosis inducer to strengthen antitumor therapy.

Author contributions

Zhiwei Zhang: data curation, investigation, and writing – original draft. Jingjing Xiang: conceptualization, data curation, investigation, and writing – review & editing. Lijiao Guan: data curation, writing – original draft, and validation. Pu Chen: investigation, methodology, and writing – review & editing. Changzhong Li: investigation, methodology, and writing – review & editing. Chunlei Guo: investigation, methodology, and writing – review & editing. Yan Hu: writing – review & editing. Saipeng Huang: conceptualization, funding acquisition, and writing – review & editing. Lintao Cai: funding acquisition, project administration, and writing – review & editing. Ping Gong: conceptualization, funding acquisition, and writing – review & editing. All authors revised and approved the text.

Conflicts of interest

There are no conflicts to declare.

Acknowledgements

References

1 N. Kang, S. Son, S. Min, H. Hong, C. Kim, J. An, J. S. Kim and H. Kang, *Chem. Soc. Rev.*, 2023, **52**, 3955–3972.

2 F. Zeng, S. Nijiati, L. Tang, J. Ye, Z. Zhou and X. Chen, *Angew. Chem., Int. Ed.*, 2023, **62**, e202300379.

3 D. Li and Y. Li, *Signal Transduction Targeted Ther.*, 2020, **5**, 108.

4 X. Jiang, B. R. Stockwell and M. Conrad, *Nat. Rev. Mol. Cell Biol.*, 2021, **22**, 266–282.

5 G. Lei, L. Zhuang and B. Gan, *Nat. Rev. Cancer*, 2022, **22**, 381–396.

6 Y. Jiang, X. Zhao, J. Huang, J. Li, P. K. Upputuri, H. Sun, X. Han, M. Pramanik, Y. Miao, H. Duan, K. Pu and R. Zhang, *Nat. Commun.*, 2020, **11**, 1857–1869.

7 R. Yue, C. Zhang, L. Xu, Y. Wang, G. Guan, L. Lei, X. Zhang and G. Song, *Chem*, 2022, **8**, 1956–1981.

8 J. D. Mancias, X. Wang, S. P. Gygi, J. W. Harper and A. C. Kimmelman, *Nature*, 2014, **509**, 105–109.

9 G. Kroemer and M. Jäättelä, *Nat. Rev. Cancer*, 2005, **5**, 886–897.

10 L. Chen, X. Sun, K. Cheng, P. D. Topham, M. Xu, Y. Jia, D. Dong, S. Wang, Y. Liu, L. Wang and Q. Yu, *Adv. Fiber Mater.*, 2022, **4**, 1669–1684.

11 F. Wang, R. Gómez-Sintes and P. Boya, *Traffic*, 2018, **19**, 918–931.

12 M. Wen, N. Yu, S. Wu, M. Huang, P. Qiu, Q. Ren, M. Zhu and Z. Chen, *Bioact. Mater.*, 2022, **18**, 242–253.

13 M. Wen, N. Yu, Z. Yi, P. Qiu, C. Tao, D. K. Macharia, M. Zhu, Z. Chen and X. Liu, *Nano Today*, 2023, **50**, 101863.

14 N. Yu, W. Tu, P. Qiu, Q. Ren, X. Chen, M. Zhu, Y. Liu and Z. Chen, *Nano Today*, 2022, **43**, 101427.

15 G. Q. Chen, F. A. Benthani, J. Wu, D. Liang, Z. X. Bian and X. Jiang, *Cell Death Differ.*, 2019, **27**, 242–254.

16 B. R. Stockwell, J. P. F. Angeli, H. Bayir, A. I. Bush, M. Conrad, S. J. Dixon, S. Fulda, S. Gascón, S. K. Hatzios, V. E. Kagan, K. Noel, X. Jiang, A. Linkermann, M. E. Murphy, M. Overholtzer, A. Oyagi, G. C. Pagnussat, J. Park, Q. Ran, C. S. Rosenfeld, K. Salnikow, D. Tang, F. M. Torti, S. V. Torti, S. Toyokuni, K. A. Woerpel and D. D. Zhang, *Cell*, 2017, **171**, 273–285.

17 S. Xu, H. Zheng, R. Ma, D. Wu, Y. Pan, C. Yin, M. Gao, W. Wang, W. Li, S. Liu, Z. Chai and R. Li, *Nat. Commun.*, 2020, **11**, 3484.

18 Y. Zhao, W. Zhao, Y. C. Lim and T. Liu, *Mol. Pharm.*, 2019, **16**, 2532–2539.

19 B. Zhang, Y. Gao, R. Yang, Z. Ouyang, H. Yu, H. Wang, X. Shi and M. Shen, *Adv. Fiber Mater.*, 2022, **4**, 807–819.

20 R. Wang, J. Wang, A. Hassan, C.-H. Lee, X.-S. Xie and X. Li, *Nat. Commun.*, 2021, **12**, 1782–1789.

21 S. Y. Zhu, R. Q. Yao, Y. X. Li, P. Y. Zhao, C. Ren, X. H. Du and Y. M. Yao, *Cell Death Dis.*, 2020, **11**, 817.

22 H. Chen, L. Xiao, Y. Anraku, P. Mi, X. Liu, H. Cabral, A. Inoue, T. Nomoto, A. Kishimura, N. Nishiyama and K. Kataoka, *J. Am. Chem. Soc.*, 2013, **136**, 157–163.

23 R. Luo, Y. Li, Q. Zhou, J. Zheng, D. Ma, P. Tang, S. Yang, Z. Qing and R. Yang, *Analyst*, 2016, **141**, 3224–3227.

24 R. M. Perera and R. Zoncu, *Annu. Rev. Cell Dev. Biol.*, 2016, **32**, 223–253.

25 J. Tian, L. Ding, H. Ju, Y. Yang, X. Li, Z. Shen, Z. Zhu, J.-S. Yu and C. J. Yang, *Angew. Chem., Int. Ed.*, 2014, **53**, 9544–9549.

26 J. Yang, L. Xu, Y. Ding, C. Liu, B. Wang, Y. Yu, C. Hui, S. Ramakrishna, J. Zhang and Y. Long, *Adv. Fiber Mater.*, 2023, **5**, 209–222.

27 X. Chen, R. Kang, G. Kroemer and D. Tang, *Nat. Rev. Clin. Oncol.*, 2021, **18**, 280–296.

28 Q. Guan, L. L. Zhou and Y. B. Dong, *J. Mater. Chem. B*, 2021, **9**, 8906–8936.

29 C. Ou, W. Na, W. Ge, H. Huang, F. Gao, L. Zhong, Y. Zhao and X. Dong, *Angew. Chem., Int. Ed.*, 2021, **60**, 8157–8163.